

# Doping against the Native Propensity of MoS<sub>2</sub>: Degenerate Hole Doping by Cation Substitution

Joonki Suh,<sup>†</sup> Tae-Eon Park,<sup>‡</sup> Der-Yuh Lin,<sup>§</sup> Deyi Fu,<sup>†</sup> Joonsuk Park,<sup>||</sup> Hee Joon Jung,<sup>⊥</sup> Yabin Chen,<sup>†</sup> Changhyun Ko,<sup>†</sup> Chaun Jang,<sup>‡</sup> Yinghui Sun,<sup>||</sup> Robert Sinclair,<sup>||</sup> Joonyeon Chang,<sup>‡</sup> Sefaattin Tongay,<sup>†,∇</sup> and Junqiao Wu<sup>\*,†,||</sup>

<sup>†</sup>Department of Materials Science and Engineering, University of California, Berkeley, California 94720, United States

<sup>‡</sup>Spin Convergence Research Center, Korea Institute of Science and Technology, Seoul 136-791, Korea

<sup>§</sup>Department of Electronics Engineering, National Changhua University of Education, Changhua 50007, Taiwan

<sup>||</sup>Department of Materials Sciences and Engineering, Stanford University, Stanford, California 94305, United States

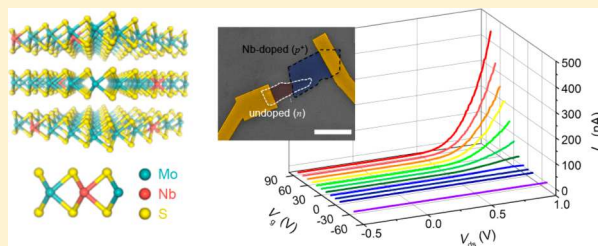
<sup>⊥</sup>Energy and Environmental Directorate, Pacific Northwest National Laboratory, Richland, Washington 99352, United States

<sup>∇</sup>Materials Sciences Division, Lawrence Berkeley National Laboratory, Berkeley, California 94720, United States

## Supporting Information

**ABSTRACT:** Layered transition metal dichalcogenides (TMDs) draw much attention as the key semiconducting material for two-dimensional electrical, optoelectronic, and spintronic devices. For most of these applications, both *n*- and *p*-type materials are needed to form junctions and support bipolar carrier conduction. However, typically only one type of doping is stable for a particular TMD. For example, molybdenum disulfide (MoS<sub>2</sub>) is natively an *n*-type presumably due to omnipresent electron-donating sulfur vacancies, and stable/controllable *p*-type doping has not been achieved. The lack of *p*-type doping hampers the development of charge-splitting *p*–*n* junctions of MoS<sub>2</sub>, as well as limits carrier conduction to spin-degenerate conduction bands instead of the more interesting, spin-polarized valence bands. Traditionally, extrinsic *p*-type doping in TMDs has been approached with surface adsorption or intercalation of electron-accepting molecules. However, practically stable doping requires substitution of host atoms with dopants where the doping is secured by covalent bonding. In this work, we demonstrate stable *p*-type conduction in MoS<sub>2</sub> by substitutional niobium (Nb) doping, leading to a degenerate hole density of  $\sim 3 \times 10^{19} \text{ cm}^{-3}$ . Structural and X-ray techniques reveal that the Nb atoms are indeed substitutionally incorporated into MoS<sub>2</sub> by replacing the Mo cations in the host lattice. van der Waals *p*–*n* homojunctions based on vertically stacked MoS<sub>2</sub> layers are fabricated, which enable gate-tunable current rectification. A wide range of microelectronic, optoelectronic, and spintronic devices can be envisioned from the demonstrated substitutional bipolar doping of MoS<sub>2</sub>. From the miscibility of dopants with the host, it is also expected that the synthesis technique demonstrated here can be generally extended to other TMDs for doping against their native unipolar propensity.

**KEYWORDS:** transition-metal dichalcogenides, molybdenum disulfide, substitutional doping, *p*-type MoS<sub>2</sub>, *p*–*n* junction



In layered transition metal dichalcogenides (TMDs), each layer is weakly bonded to its neighbors by van der Waals forces, thereby allowing physical or chemical isolation into atomically thin semiconducting layers, as well as assembly of junctions free of lattice mismatch issues. A wide variety of TMDs have been used as the active material to fabricate atomically thin field-effect transistors (FETs),<sup>1,2</sup> integrated circuits,<sup>3,4</sup> and optoelectronic devices<sup>5–7</sup> such as light-emitting diodes, solar cells, and photodiodes.

Similar to traditional semiconductor technologies, stable *n*- and *p*-type conduction in the TMDs is indispensable for all these applications. Yet in contrast, a bipolar doping strategy of the TMDs is currently lacking. Wisdom can be learned from studies of conventional semiconductors, where a native, unipolar doping propensity is usually found. For example, in

semiconductors such as CdO and InAs whose conduction band minimum (CBM) and valence band maximum (VBM) lie low with respect to the vacuum level, native *n*-type conduction and difficulty in *p*-type doping are observed; the opposite is true for semiconductors such as Ge and diamond whose CBM and VBM lie high. This is attributed to the amphoteric doping behavior of electrically active native point defects,<sup>8</sup> such as vacancies, interstitials, and defect complexes, which naturally occur in the materials in thermodynamic equilibrium. Extending this understanding to TMDs,<sup>9</sup> it would be natural to predict a native *n*-type (*p*-type) behavior of not intentionally

**Received:** August 24, 2014

**Revised:** November 18, 2014

**Published:** November 24, 2014

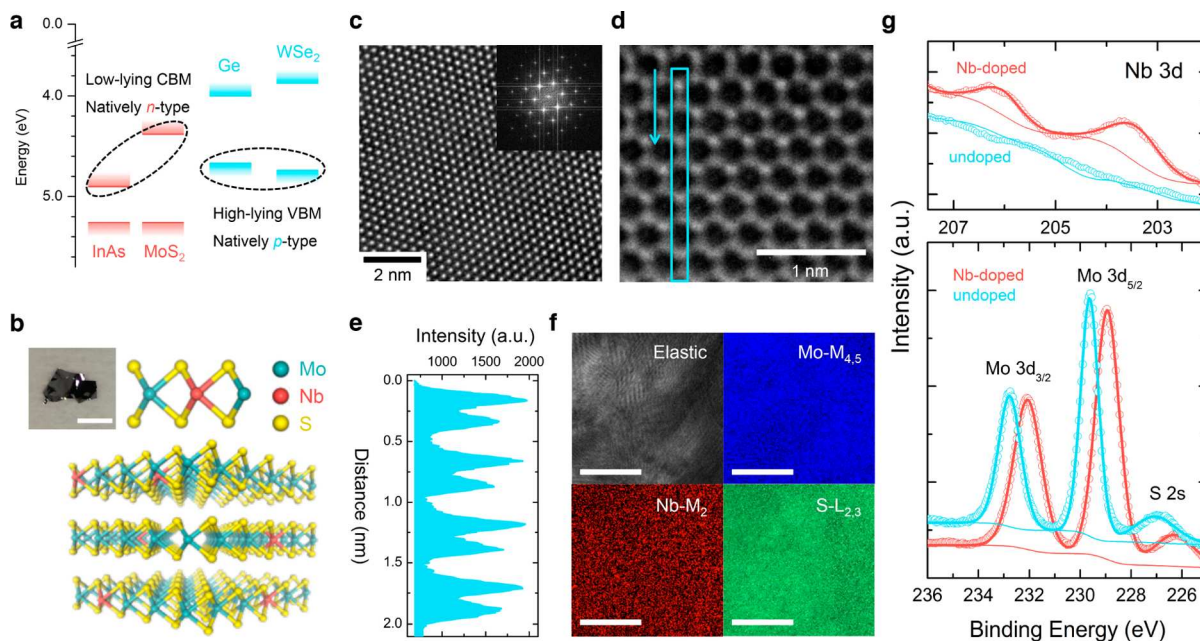


**Figure 1.** Structural and chemical analyses of Nb-doped MoS<sub>2</sub> (MoS<sub>2</sub>:Nb). (a) Band-edge (CBM and VBM) alignment of representative conventional semiconductors and TMDs, referenced to the vacuum level. (b) Cross-section illustration of van der Waals coupled MoS<sub>2</sub>:Nb layers where Nb dopants replace the Mo host atoms in a substitutional manner. A digital photograph inset shows a synthesized MoS<sub>2</sub>:Nb crystal with a scale bar of 3 mm. (c) HRTEM image of the MoS<sub>2</sub>:Nb with the corresponding FFT in the inset. (d) Cs (spherical aberration)-corrected HRTEM image with subangstrom resolution acquired from the monolayer part. (e) Transmitted electron intensity along the vertical direction of corresponding blue box denoted in panel d. (f) EFTEM-SI maps of elastic (0 eV), Mo M<sub>4,5</sub>, Nb M<sub>2</sub>, and S L<sub>2,3</sub> measured from the same region of the MoS<sub>2</sub>:Nb sample. Scale bars are 100 nm. (g) XPS scans of the Nb 3d (top), the Mo 3d, and S 2s (both in bottom) core-levels measured from the Nb-doped and undoped MoS<sub>2</sub>.

doped MoS<sub>2</sub> (WSe<sub>2</sub>), given the low (high)-lying CBM and VBM in MoS<sub>2</sub> (WSe<sub>2</sub>) as seen in Figure 1a.

Currently, modulation of carrier type and density in these layered TMDs is achieved by means of electrostatic FET gating,<sup>7,10</sup> metal work-function engineering,<sup>11,12</sup> surface functionalization,<sup>13,14</sup> or charge transfer from physic-sorbed volatile molecules.<sup>15</sup> However, to dope TMDs against their natural doping propensity, such as *p*-type in MoS<sub>2</sub> (*n*-type in WS<sub>2</sub>) with very low VBM (high CBM), it is challenging to find molecules capable of donating holes (electrons) effectively to these low (high) - lying band edges. Moreover, practical applications require substitution of host atoms with dopants as practiced in traditional semiconductors, where the doping is secured and stabilized by covalent bonding inside the lattice. Heterojunctions integrating different materials, such as *n*-type MoS<sub>2</sub> with *p*-type WSe<sub>2</sub>,<sup>16,17</sup> have been fabricated as an alternative to homojunctions, but these heterostructures usually suffer from their type-II band offset. For example, it leads to lower photovoltages because the band offset curtails the maximum splitting of Fermi levels, as well as red-shifted light emission due to recombination across the spatially indirect band edges.<sup>18,19</sup>

Indeed, for MoS<sub>2</sub>, consistent with the prediction above, recent electrical<sup>1–4,16,17</sup> and optical<sup>20</sup> investigations confirm its native *n*-doping, owing hypothetically to sulfur vacancies.<sup>21,22</sup> The lack of *p*-type doping strictly limits carrier conduction in MoS<sub>2</sub> to its conduction bands, despite the suggestion that *p*-type operation is more desirable for MoS<sub>2</sub>-based FET devices,<sup>10</sup> and much more interest lies in its spin-polarized valence bands for the recently developed valleytronics.<sup>23,24</sup> Niobium (Nb), which has one less valence electron than Mo, is theoretically suggested as the most suitable substitutional acceptor by

density-functional energetics/formation energies calculations.<sup>25</sup> Moreover, MoS<sub>2</sub> and NbS<sub>2</sub> share the identical 2H crystal structure, with similar lattice parameters,  $a = 3.16$  and  $3.32$  Å and  $c = 12.29$  and  $11.94$  Å for MoS<sub>2</sub> and NbS<sub>2</sub>, respectively.<sup>26</sup> The covalent radius (Mo = 130 pm and Nb = 134 pm)<sup>27</sup> and oxidation states of Mo and Nb in the 2H-polytype lattice are nearly identical. Indeed, fullerene-like Mo<sub>x</sub>Nb<sub>1-x</sub>S<sub>2</sub> nanoparticles<sup>28</sup> and polycrystalline thin-films<sup>29</sup> have been reported, but unambiguous *p*-type conduction and direct evidence of the substitutionality of doping have not been demonstrated in single-crystal MoS<sub>2</sub>. In this work, we report stable *p*-type conduction in MoS<sub>2</sub> single crystals and ultrathin layers via substitutional Nb doping. The substitutionality of the Nb dopants in the MoS<sub>2</sub> crystals is confirmed by structural and chemical analysis techniques, and the degenerate *p*-type conduction is evaluated by Hall-effect and gated transport studies. Prototypical *p*-*n* homojunctions built from vertically stacked MoS<sub>2</sub> layers show current rectification tunable by a gate voltage.

**Results and Discussions.** The Nb-doped MoS<sub>2</sub> (MoS<sub>2</sub>:Nb) single crystals were grown by a chemical vapor transport (CVT) method using iodine as the transport agent, an approach that has been employed to prepare other layered compounds with high quality.<sup>30,31</sup> A horizontal three-zone furnace was utilized where the high (low) temperature zone was used as the reaction (growth) zone, as seen in Supporting Information Figure S1. Prior to the crystal growth, a quartz tube containing the transport agent and the elements required for the doped crystals was evacuated to below 10<sup>-6</sup> Torr and securely sealed. The purity of the source materials was Mo 99.99%, S 99.99%, and Nb 99.99%, with a molar ratio of Mo:S:Nb equal to 1:2:0.005 for a nominal 0.5% Nb doping.

The sealed quartz tube was then inserted into the three-zone furnace. In the beginning, the temperature of the growth zone was set to 1000 °C for 12 h to remove any possible residues. The process of the CVT was initiated with a temperature gradient varying from 1050 °C in the reaction zone to 935 °C in the growth zone over a distance of  $\sim 30$  cm, and the system was held in this condition over 500 h in order to provide sufficient diffusion and equilibration for the single-crystal synthesis. The CVT growth yielded large, thin, and shiny  $\text{MoS}_2\text{:Nb}$  crystals that are typically a few millimeters in lateral size with high crystallinity (Figure 1b). Similar to other TMDs, these as-synthesized  $\text{MoS}_2\text{:Nb}$  crystals are exfoliation-ready, and the number of exfoliated layers can be determined by Raman spectroscopy and atomic force microscopy (Supporting Information Figure S2).

To determine the crystal structure and evaluate the crystallinity of the  $\text{MoS}_2\text{:Nb}$ , we deployed extensive high-resolution transmission electron microscopy (HRTEM) measurements over a wide area on multiple samples. The as-synthesized  $\text{MoS}_2\text{:Nb}$  is single crystalline, exhibiting a hexagonal lattice as seen from the fast-Fourier transform (FFT) pattern displayed in the inset of Figure 1c (see also selected area electron diffraction pattern in Supporting Information Figure S3a). The estimated lattice spacing of 1.6 and 2.7 Å, corresponding to the (110) and (100) planes, respectively, is consistent with reported values.<sup>32</sup> Cross-sectional HRTEM images also show highly parallel layer stacking with an interlayer separation of approximately 6.15 Å (Supporting Information Figure S3b). The Cs (spherical aberration)-corrected atomic HRTEM image in Figure 1d clearly reveals hexagonal rings formed by the S atoms (dimmer sites) together with the transition metal atoms, the Mo atoms or Nb dopants (brighter sites) supported by the corresponding intensity profiles presented in Figure 1e. It is noted that structural imperfections such as grain boundaries, dislocations, and atomic defects were not observed from the HRTEM. Energy-filtered electron transmission microscopy spectrum imaging (EFTEM-SI) was subsequently used to probe the chemical composition of the  $\text{MoS}_2\text{:Nb}$  with nanoscale spatial resolution, in particular, the incorporation of Nb dopants into the lattice. As seen in Figure 1f, the Nb signal was well resolved through its  $M_2$  peak ( $\sim 378$  eV) and is indeed uniformly dispersed in the  $\text{MoS}_2$  matrix with no evidence of clustering (also see the corresponding electron energy loss spectrum in Supporting Information Figure S3c).

The Nb dopants in the  $\text{MoS}_2$  crystals were further analyzed with X-ray photoelectron spectroscopy (XPS). Distinct binding energy peaks associated with the Nb 3d core levels at 203.6 and 206.1 eV were detected only in the  $\text{MoS}_2\text{:Nb}$  samples (Figure 1g), and they well match previously observed XPS features from fullerene-like  $\text{Mo}_{1-x}\text{Nb}_x\text{S}_2$  nanoparticles.<sup>28</sup> In addition, the core-level peaks of Mo and S in the  $\text{MoS}_2\text{:Nb}$  show a uniform shift toward lower binding energies compared to those of the undoped  $\text{MoS}_2$ . This shift is attributed to lowering of the Fermi level ( $E_F$ ) upon the  $p$ -type doping, as similarly observed in previous studies.<sup>28,33</sup> The amount of  $E_F$  downshift,  $\sim 0.7$  eV, is found to be consistent with the  $\text{MoS}_2$  band gap of 1.2 eV<sup>34</sup> and the degenerate  $p$ -doping.

Recent reports have suggested many possible, nonsubstitutional atomic configurations for dopants in  $\text{MoS}_2$ , for example, adatom<sup>35</sup> or intercalation.<sup>36</sup> Therefore, it is important to evaluate the substitutionality of Nb in the  $\text{MoS}_2$  lattice. Because Nb and Mo atoms are adjacent to each other on the periodic

table, it is rather difficult to distinguish them in the HRTEM, and more chemically sensitive characterization techniques are required to determine the location of Nb dopants. Extended X-ray absorption fine structure (EXAFS) analysis is ideally suited for this purpose, allowing for determination of local environment around the X-ray absorbing atoms. By analyzing oscillations in the normalized X-ray absorption data,<sup>37,38</sup> critical information can be extracted, such as local coordination number ( $N$ ), interatomic distance to neighboring atoms ( $r$ ), and the Debye–Waller disorder parameter ( $\sigma^2$ ). Despite their adjacent atomic numbers, the  $K$  edge energies of Nb and Mo are widely separated by  $\sim 1$  keV (Nb = 18.99 keV and Mo = 20.01 keV), and this provides sufficient energy span to fully resolve their EXAFS oscillations in the postabsorption spectral region. Figure 2a shows the normalized absorption data for the

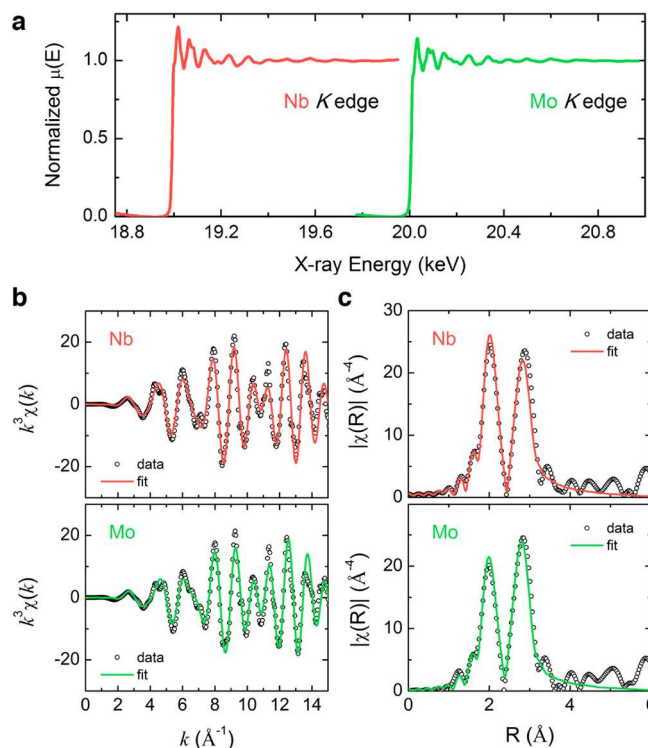


**Figure 2.** EXAFS analysis on Nb-doped  $\text{MoS}_2$ : Evidence for substitutional doping. (a) Raw X-ray absorption data for the Nb and Mo  $K$  edges normalized by peak intensity. (b) EXAFS oscillations extracted from the absorption data weighted by  $k^3$ . (c) Radial distribution of Fourier-transformed EXAFS signal. Points are raw experimental data while red and green lines are best fits for the Nb and Mo  $K$  edge, respectively.

Nb and Mo  $K$  edges, collected in the fluorescence and transmission mode, respectively. Figure 2b shows the extracted EXAFS oscillations,  $k^3$ -weighted  $\chi(k)$ , along with the result of best fitting to the data. The fitting was determined by Fourier transforming the  $\chi(k)$  across a  $k$ -range up to  $15 \text{ \AA}^{-1}$  considering the first two coordination shells for both the Nb and Mo  $K$  edges (see detailed fitting parameters in the Supporting Information).

The results show nearly identical  $N$  and  $r$ , and thus local atomic bonding environment for the Nb and Mo atoms, clearly indicating the substitutional nature of Nb atoms. The Fourier transformed  $k^3$ -weighted EXAFS is plotted in Figure 2c showing two distinct peaks at two radial distances. The first

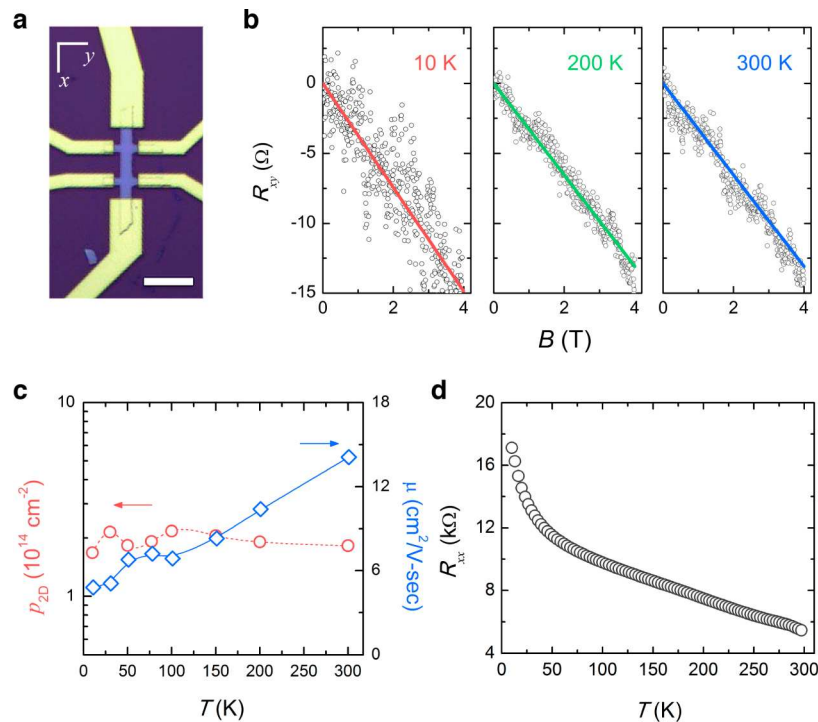


**Figure 3.** Hall-effect measurement of MoS<sub>2</sub>:Nb microdevices. (a) Optical microscopy image of a Hall-bar device based on a multilayer (61 nm thick, determined by atomic force microscopy) MoS<sub>2</sub>:Nb flake (Scale bar = 10  $\mu\text{m}$ ). (b) Hall resistance,  $R_{xy}$ , as a function of magnetic field at three representative temperatures (10, 200, and 300 K). Blank circles and colored lines are the measured data and linear fits, respectively. (c) Calculated hole sheet concentration (red) and Hall-effect mobility (blue) as a function of temperature from 10 to 300 K. (d) Longitudinal resistance  $R_{xx}$  of the Hall-bar device as a function of temperature.

peak corresponds to atomic bonds with S atoms, the nearest neighbor of the transition metal atoms, and the second peak is associated with intralayer cation (transition metal) neighbors. These bond lengths agree quantitatively with those measured in MoS<sub>2</sub> single crystals.<sup>39</sup> Here, though scattering from the first and second nearest neighbors of the X-ray absorbing cation atoms is evident, the existence of the interlayer van der Waals gap may damp contributions from neighbors at greater distances. We also note that  $\sigma^2$  is quite narrow, despite that the data was collected in ambient air at 300 K, which further confirms the high crystal quality in agreement with the HRTEM measurements.

We measured the  $p$ -type electrical conduction in a thin flake mechanically exfoliated from the MoS<sub>2</sub>:Nb crystals using variable-temperature Hall effect. The multilayer MoS<sub>2</sub>:Nb Hall device was fabricated on a 300 nm SiO<sub>2</sub>/Si substrate, and standard e-beam lithography (EBL) was used to define the flake into a Hall bar configuration as seen in Figure 3a. After etching the unwanted area with XeF<sub>2</sub> gas, a second EBL was performed to pattern the voltage leads and current injection electrodes, followed by deposition of Ti/Au (5/100 nm) metal contacts (see experimental details in the Supporting Information). As shown in Supporting Information Figure S4, two-probe  $I$ - $V$  curves displayed linear characteristics, suggesting ohmic contacts, despite the Schottky barrier expected between the MoS<sub>2</sub> valence band and Ti (surface potential-energy barrier  $\Phi_B \sim 1.0$  eV, estimated from the Ti work function 4.33 eV and the VBM of MoS<sub>2</sub> (ref 9)). This is attributed to the degenerate  $p$ -type doping resulting in very narrow depletion width of a few nanometers, thereby allowing significant tunneling current to flow as typically occurring in heavily doped semiconductors.<sup>40,41</sup>

The measured Hall resistance,  $R_{xy}$ , is plotted as a function of the magnetic field ( $B$ ) in Figure 3b. The magnetic field was varied up to 4 T, and both current injection directions were used in order to remove influence of possible misalignment of voltage electrodes from the longitudinal resistance  $R_{xx}$ ; that is, the treatment is equivalent to  $R_{xy}(B) = (V_{xy}(+B) - V_{xy}(-B))/2I_{xxx}$ .<sup>42</sup> The results confirm the  $p$ -type conduction of MoS<sub>2</sub>:Nb, as well as reveal a constancy of the Hall coefficient  $R_H (= R_{xy}/B = -1/p_{2D}e)$  over a wide range of temperature. Linear fitting in Figure 3b yields a high sheet hole concentration ( $p_{2D}$ ) of  $1.8 \times 10^{14} \text{ cm}^{-2}$ , corresponding to a bulk concentration of  $3.0 \times 10^{19} \text{ cm}^{-3}$ , far exceeding the critical hole concentration for degenerate  $p$ -type doping in MoS<sub>2</sub> (see Supporting Information). The absence of carrier freeze-out (Figure 3c) indicates a degenerate level of doping, and such a dense hole concentration in the degenerate limit is indeed in good agreement with the nominal doping concentration of Nb as analyzed below, suggesting the tunability of the doping level with varying the dopant concentration. Using the assumption that each of the Nb atoms acts as a single acceptor,<sup>27</sup>  $p_{2D}^{\text{nominal}}$  is estimated from the 0.5% Nb doping to be  $\sim 2.8 \times 10^{14} \text{ cm}^{-2}$ , showing good consistency with the measured  $p_{2D}$  considering the unknown degree of charge compensation by the donor-like sulfur vacancies. We also note that a nearly identical hole density is observed from another Hall device. Combined with the four-terminal  $R_{xx}$  data presented in Figure 3d and geometrical factors of the Hall device, the Hall mobility ( $\mu$ ) was extracted, which shows a monotonic increase with temperature. This is a further signature of degenerately doped semiconductors,<sup>43</sup> where ionized impurity scattering dominates over phonon scattering even at room temperature. This is the opposite to the behavior of intrinsic MoS<sub>2</sub> crystals, where acoustic phonon

scattering plays a much greater role in limiting  $\mu$  at room temperature.<sup>2</sup>

To demonstrate a proof-of-concept device application of the substitutionally doped MoS<sub>2</sub>, we fabricated a  $p$ - $n$  homojunction. First, back-gated FETs using Nb-doped and undoped MoS<sub>2</sub> flakes were separately fabricated, and typical electrical transport characteristics are presented in Figure 4a. The

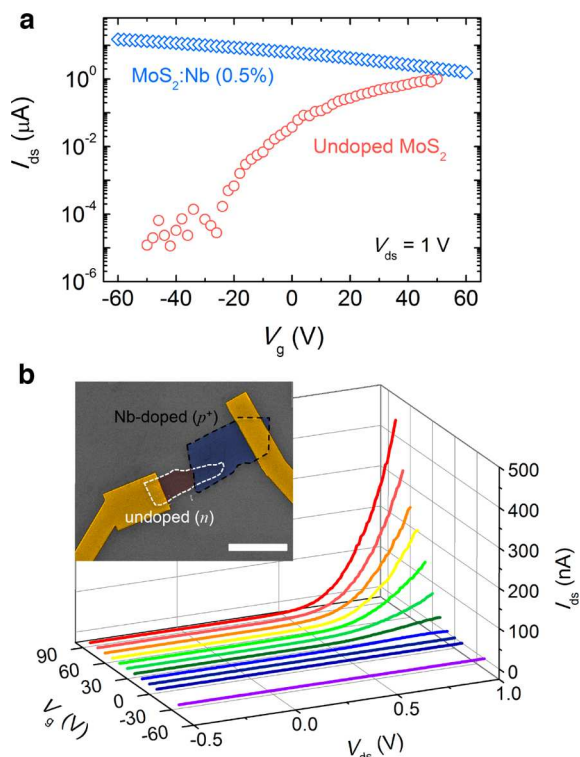


**Figure 4.** Gate-tunable rectification across a van der Waals MoS<sub>2</sub>  $p$ - $n$  junction. (a) Gate voltage ( $V_g$ ) dependence of channel current of multilayer MoS<sub>2</sub>:Nb and undoped MoS<sub>2</sub> devices at a bias voltage ( $V_{ds}$ ) of 1 V. Ti/Au was used for the source (s) and drain (d) contacts. (b)  $I$ - $V$  characteristic at variable back-gate voltages measured across the van der Waals  $p$ - $n$  junction assembled with MoS<sub>2</sub>:Nb (60 nm) and undoped MoS<sub>2</sub> (4 nm). Inset is a false-color scanning electron microscopy image along with a scale bar of 10  $\mu\text{m}$ .

undoped, few-layer FET shows a strong,  $n$ -type gate voltage ( $V_g$ ) dependence in the source-drain current ( $I_{ds}$ ). In contrast, the MoS<sub>2</sub>:Nb device exhibits a drastically different behavior with a  $p$ -type conduction, a much weaker  $V_g$  dependence, and much higher on-current. The weak  $V_g$  dependence of the MoS<sub>2</sub>:Nb device is similar to recent observations from degenerately  $n$ -type doped MoS<sub>2</sub> crystals,<sup>44</sup> further confirming the degeneracy of our Nb doping level.

Next, a vertically stacked  $p$ - $n$  junction was formed by overlaying a multilayer MoS<sub>2</sub>:Nb flake onto a few-layer, undoped MoS<sub>2</sub>, as shown in the inset of Figure 4b. The sample was then mildly annealed to enhance the interlayer coupling<sup>45</sup> between the van der Waals  $p$ - $n$  interface. Ti/Au layers were deposited again for achieving ohmic contacts with both the MoS<sub>2</sub>:Nb and undoped MoS<sub>2</sub>. Such vertically stacked device architecture has been recently shown to be able to support high current densities and offer superior tunability of the junction current.<sup>46</sup> The resultant  $p$ - $n$  homojunction exhibits excellent rectification characteristics as shown in Figure 4b. Remarkably, the degree of rectification is tunable by

modulating the density of free carriers in the bottom  $n$ -type layer with electrostatic field from the back gate. In such asymmetric  $p^+$ - $n$  junction devices, the rectification properties are predominantly governed by the lightly doped  $n$ -side in which the depletion layer extends. While the heavily  $p$ -doped MoS<sub>2</sub>:Nb is relatively insensitive to  $V_g$ , the density of electrons in the undoped  $n$ -side rapidly increases upon more positive  $V_g$ , leading to much enhanced current flow (see a qualitative band diagram in the Supporting Information). This unique, tunable rectification of current is fully reversible with respect to variation of  $V_g$ , indicating the operation stability and durability.

Notably, the fabricated Hall devices and  $p$ - $n$  junctions are stable in ambient air even without additional treatment such as capping layer protection, with only minimal changes in the  $R_{xx}$  and  $I$ - $V$  characteristics over time (Supporting Information Figure S6). This is in stark contrast to the existing approach of using molecular doping,<sup>13,14,47,48</sup> which usually suffers from volatility and reactivity with air or water molecules. This superior stability is due to the covalently bonded, substitutional dopants, similar to those previously observed in graphene<sup>49</sup> (for example, long-term operational stability of nitrogen-doped graphene as an electrode in fuel cells<sup>50</sup>). Our results also show that, thanks to the degeneracy and bipolarity of doping, one can achieve a wide tunability of current rectification as compared to the recently reported  $p$ - $n$  diodes built from type-II heterojunctions.<sup>16,17</sup> Moreover, distinct metals with particular work functions are not needed in making contact with the MoS<sub>2</sub> homojunction devices, thus simplifying the device fabrication process.

As the VBM of MoS<sub>2</sub> is located at  $\sim 5.4$  eV, well below the vacuum level, it is challenging to find proper metals and surface-adsorbed molecules with high reduction potentials to donate holes to the VBM. Therefore, only the atomic substitution method demonstrated in this work can stabilize effective, high-density of hole doping in MoS<sub>2</sub>. On the other hand, ab initio computations have predicted that both Nb (for  $p$ -type) and Re (for  $n$ -type) dopants are thermodynamically miscible on the cation site in MoX<sub>2</sub> and WX<sub>2</sub> at high temperatures, where X represents the chalcogen anion.<sup>25</sup> Therefore, it is expected that the CVT synthesis technique demonstrated in this work can be readily extended to doping other TMDs. To this end, a general cation substitution strategy can be developed to dope all TMDs against their native unipolar doping propensity, so as to achieve bipolar doping in these TMDs.

In summary, we demonstrate a substitutional cation doping strategy in which degenerately high concentrations of free carriers are introduced in the host TMDs with covalently bonded dopants. The strategy is superior in terms of versatility and stability over other doping methods based on adsorption or intercalation of volatile species. Given the native  $n$ -type conduction in MoS<sub>2</sub>, the stable  $p$ -type doping is of great importance for device applications and also provides a materials platform to explore and exploit the spin-polarized valence bands of MoS<sub>2</sub>.

## ■ ASSOCIATED CONTENT

### 📄 Supporting Information

Experimental details including HRTEM, EFTEM-SI, XPS, and EXAFS measurements, device fabrication, and electrical transport characterization. Raman spectra and additional HRTEM analysis of the MoS<sub>2</sub>:Nb crystals. Details of EXAFS fitting parameters. Band diagrams and stability studies of the

fabricated devices. This material is available free of charge via the Internet at <http://pubs.acs.org>.

## AUTHOR INFORMATION

### Corresponding Author

\* E-mail: [wuj@berkeley.edu](mailto:wuj@berkeley.edu).

### Present Address

<sup>†</sup>School for Engineering of Matter, Transport and Energy, Arizona State University, Tempe, Arizona 85287, United States.

### Author Contributions

The manuscript was written through contributions of all authors. All authors have given approval to the final version of the manuscript.

### Notes

The authors declare no competing financial interest.

## ACKNOWLEDGMENTS

This work was supported by the National Science Foundation under Grant No. DMR-1306601. J.W. and Y.C. acknowledge support from the Singapore-Berkeley Research Initiative for Sustainable Energy (SinBeRISE). T.-E.P., C.J., and J.C. were supported by KIST Institutional program. D.-Y.L. acknowledges support by the National Science Council of Taiwan under Grant No. NSC 102-2112-M-018-002. Use of the Stanford Synchrotron Radiation Light source (SLAC National Accelerator Laboratory) and XPS at the Molecular Foundry is supported by the U.S. Department of Energy, Office of Science, Office of Basic Energy Sciences under Contract No. DE-AC02-76SF00515 and DE-AC02-05CH11231, respectively. We thank Dr. D. Frank Ogletree, Erik J. Nelson, and Junko Yano for assistance with XPS and EXAFS measurements, Dr. Yeonbae Lee for the transport measurements, and Prof. Mike Crommie for use of the alignment microscope. Use of the FEI Titan 80-300 ETEM at Stanford Nanocharacterization Lab and JEOL ARM 200cF at the Pacific Northwest National Lab are also acknowledged.

## REFERENCES

- Radisavljevic, B.; Radenovic, A.; Brivio, J.; Giacometti, V.; Kis, A. *Nat. Nanotechnol.* **2011**, *6*, 147–150.
- Kim, S.; Konar, A.; Hwang, W.-S.; Lee, J. H.; Lee, J.; Yang, J.; Jung, C.; Kim, H.; Yoo, J.-B.; Choi, J.-Y.; Jin, Y. W.; Lee, S. Y.; Jena, D.; Choi, W.; Kim, K. *Nat. Commun.* **2012**, *3*, 1011.
- Radisavljevic, B.; Whitwick, M. B.; Kis, A. *ACS Nano* **2011**, *5*, 9934–9938.
- Wang, H.; Yu, L.; Lee, Y.-H.; Shi, Y.; Hsu, A.; Chin, M. L.; Li, L.-J.; Dubey, M.; Kong, J.; Palacios, T. *Nano Lett.* **2012**, *12*, 4674–4680.
- Pospischil, A.; Furchi, M. M.; Mueller, T. *Nat. Nanotechnol.* **2014**, *9*, 257–261.
- Baughner, B. W. H.; Churchill, H. O. H.; Yang, Y.; Jarillo-Herrero, P. *Nat. Nanotechnol.* **2014**, *9*, 262–267.
- Ross, J. S.; Klement, P.; Jones, A. M.; Ghimire, N. J.; Yan, J.; Mandrus, D. G.; Taniguchi, T.; Watanabe, K.; Kitamura, K.; Yao, Y.; Cobden, D. H.; Xu, X. *Nat. Nanotechnol.* **2014**, *9*, 268–272.
- Walukiewicz, W. *Physica B* **2001**, *302–303*, 123–134.
- Kang, J.; Tongay, S.; Zhou, J.; Li, J.; Wu, J. *Appl. Phys. Lett.* **2013**, *102*, 012111.
- Zhang, Y. J.; Ye, J. T.; Yomogida, Y.; Takenobu, T.; Iwasa, Y. *Nano Lett.* **2013**, *13*, 3023–3028.
- Chuang, S.; Battaglia, C.; Azcatl, A.; McDonnell, S.; Kang, J. S.; Yin, X.; Tosun, M.; Kapadia, R.; Fang, H.; Wallace, R. M.; Javey, A. *Nano Lett.* **2014**, *14*, 1337–1342.
- Fontana, M.; Deppe, T.; Boyd, A. K.; Rinzan, M.; Liu, A. Y.; Paranjape, M.; Barbara, P. *Sci. Rep.* **2013**, *3*, 1634.

- Mouri, S.; Miyauchi, Y.; Matsuda, K. *Nano Lett.* **2013**, *13*, 5944–5948.
- Lin, J. D.; Han, C.; Wang, F.; Wang, R.; Xiang, D.; Qin, S.; Zhang, X.-A.; Wang, L.; Zhang, H.; Wee, A. T. S.; Chen, W. *ACS Nano* **2014**, *8*, 5323–5329.
- Tongay, S.; Zhou, J.; Ataca, C.; Liu, J.; Kang, J. S.; Matthews, T. S.; You, L.; Li, J.; Grossman, J. C.; Wu, J. *Nano Lett.* **2013**, *13*, 2831–2836.
- Lee, C.-H.; Lee, G.-H.; Van der Zande, A. M.; Chen, W.; Li, Y.; Han, M.; Cui, X.; Arefe, G.; Nuckolls, C.; Heinz, T. F.; Guo, J.; Hone, J.; Kim, P. *Nat. Nanotech.* **2014**, advanced online publication (DOI: 10.1038/nnano.2014.150).
- Fang, H.; Battaglia, C.; Carraro, C.; Nemsak, S.; Ozdol, B.; Kang, J. S.; Bechtel, H. A.; Desai, S. B.; Kronast, F.; Unal, A. A.; Conti, G.; Conlon, C.; Palsson, G. K.; Martin, M. C.; Minor, A. M.; Fadley, C. S.; Yablonovitch, E.; Maboudian, R.; Javey, A. *Proc. Natl. Acad. Sci. U.S.A.* **2014**, *111*, 6198–6202.
- Borys, N. J.; Walter, M. J.; Huang, J.; Talapin, D. V.; Lupton, J. M. *Science* **2010**, *330*, 1371–1374.
- Seidel, W.; Titkov, A.; André, J. P.; Voisin, P.; Voos, M. *Phys. Rev. Lett.* **1994**, *73*, 2356–2359.
- Mak, K. F.; He, K. L.; Lee, C.; Lee, G. H.; Hone, J.; Heinz, T. F.; Shan, J. *Nat. Mater.* **2013**, *12*, 207–211.
- Qiu, H.; Xu, T.; Wang, Z.; Ren, W.; Nan, H.; Ni, Z.; Chen, Q.; Yuan, S.; Miao, F.; Song, F.; Long, G.; Shi, Y.; Sun, L.; Wang, J.; Wang, X. *Nat. Commun.* **2013**, *4*, 2642.
- Tongay, S.; Suh, J.; Ataca, C.; Fan, W.; Luce, A.; Kang, J. S.; Liu, J.; Ko, C.; Raghunathanan, R.; Zhou, J.; Ogletree, F.; Li, J.; Grossman, J. C.; Wu, J. *Sci. Rep.* **2013**, *3*, 2657.
- Mak, K. F.; He, K.; Shan, J.; Heinz, T. F. *Nat. Nanotechnol.* **2012**, *7*, 494–498.
- Suzuki, R.; Sakano, M.; Zhang, Y. J.; Akashi, R.; Morikawa, D.; Harasawa, A.; Yaji, K.; Kuroda, K.; Miyamoto, K.; Okuda, T.; Ishizaka, K.; Arita, R.; Iwasa, Y. *Nat. Nanotechnol.* **2014**, *9*, 611–617.
- Dolui, K.; Rungger, I.; Pemmaraju, C. D.; Sanvito, S. *Phys. Rev. B* **2013**, *88*, 075420.
- Wilson, J. A.; Yoffe, A. D. *Adv. Phys.* **1969**, *18*, 193–335.
- Ivanovskaya, V. V.; Zobelli, A.; Gloter, A.; Brun, N.; Serin, V.; Colliex, C. *Phys. Rev. B* **2008**, *78*, 134104.
- Deepak, F. L.; Cohen, H.; Cohen, S.; Feldman, Y.; Popovitz-Biro, R.; Azulay, D.; Millo, O.; Tenne, R. *J. Am. Chem. Soc.* **2007**, *129*, 12549–12562.
- Laskar, M. R.; Nath, D. N.; Ma, L.; Lee, E. W.; II; Lee, C. H.; Kent, T.; Yang, Z.; Mishra, R.; Roldan, M. A.; Idrobo, J.-C.; Pantelides, S. T.; Pennycook, S. J.; Myers, R. C.; Wu, Y.; Rajan, S. *Appl. Phys. Lett.* **2014**, *104*, 092104.
- Tongay, S.; Sahin, H.; Ko, C.; Luce, A.; Fan, W.; Liu, K.; Zhou, J.; Huang, Y.-S.; Ho, C.-H.; Yan, J.; Ogletree, D. F.; Aloni, S.; Ji, J.; Li, S.; Li, J.; Peeters, F. M.; Wu, J. *Nat. Commun.* **2014**, *5*, 3252.
- Tongay, S.; Narang, D. S.; Kang, J.; Fan, W.; Ko, C.; Luce, A. V.; Wang, K. X.; Suh, J.; Patel, K. D.; Pathak, V. M.; Li, J.; Wu, J. *Appl. Phys. Lett.* **2014**, *104*, 012101.
- Lee, Y.-H.; Zhang, X.-Q.; Zhang, W.; Chang, M.-T.; Lin, C.-T.; Chang, K.-D.; Yu, Y.-C.; Wang, J. T.-W.; Chang, C.-S.; Li, L.-J.; Lin, T.-W. *Adv. Mater.* **2012**, *24*, 2320–2325.
- McDonnell, S.; Addou, R.; Buie, C.; Wallace, R. M.; Hinkle, C. L. *ACS Nano* **2014**, *8*, 2880–2888.
- Kam, K. K.; Parkinson, B. A. *J. Phys. Chem.* **1982**, *86*, 463–467.
- Lin, Y.-C.; Dumcenco, D. O.; Komsa, H.-P.; Niimi, Y.; Krasheninnikov, A. V.; Huang, Y.-S.; Suenaga, K. *Adv. Mater.* **2014**, *26*, 2857–2861.
- Remskar, M.; Skraba, Z.; Stadelmann, P.; Levy, F. *Adv. Mater.* **2000**, *12*, 814–818.
- Levander, A. X.; Yu, K. M.; Novikov, S. V.; Liliental-Weber, Z.; Foxon, C. T.; Dubon, O. D.; Wu, J.; Walukiewicz, W. *J. Appl. Phys.* **2013**, *113*, 243505.
- Metha, A.; Nelson, E. J.; Webb, S. M.; Holt, J. K. *Adv. Mater.* **2009**, *21*, 102–106.

- (39) Joensen, P.; Crozier, E. D.; Alberding, N.; Frindt, R. F. *J. Phys. C: Solid State Phys.* **1987**, *20*, 4043–4053.
- (40) Baca, A. G.; Ren, F.; Zolper, J. C.; Briggs, R. D.; Pearton, S. J. *Thin Solid Films* **1997**, *308–309*, 599–606.
- (41) Park, T.-E.; Min, B.-C.; Kim, I.; Yang, J.-E.; Jo, M.-H.; Chang, J.; Choi, H.-J. *Nano Lett.* **2011**, *11*, 4730–4735.
- (42) Pradhan, N. R.; Rhodes, D.; Xin, Y.; Memaran, S.; Bhaskaran, L.; Siddiq, M.; Hill, S.; Ajayan, P. M.; Balicas, L. *ACS Nano* **2014**, No. 10.1021/nn501693d.
- (43) Bauer, G.; Kahlert, H. *Phys. Rev. B* **1972**, *5*, 566–579.
- (44) Kiriya, D.; Tosun, M.; Zhao, P.; Kang, J. S.; Javey, A. *J. Am. Chem. Soc.* **2014**, *136*, 7853–7856.
- (45) Tongay, S.; Fan, W.; Kang, J.; Park, J.; Koldemir, U.; Suh, J.; Narang, D. S.; Liu, K.; Ji, J.; Li, J.; Sinclair, R.; Wu, J. *Nano Lett.* **2014**, *14*, 3185–3190.
- (46) Yu, W. J.; Liu, Y.; Zhou, H.; Yin, A.; Li, Z.; Huang, Y.; Duan, X. *Nat. Nanotechnol.* **2013**, *8*, 952–958.
- (47) Fang, H.; Tosun, M.; Seol, G.; Chang, T. C.; Takei, K.; Guo, J.; Javey, A. *Nano Lett.* **2013**, *13*, 1991–1995.
- (48) Fang, H.; Chuang, S.; Chang, T. C.; Takei, K.; Takahashi, T.; Javey, A. *Nano Lett.* **2012**, *12*, 3788–3792.
- (49) Liu, H.; Liu, Y.; Zhu, D. *J. Mater. Chem.* **2011**, *21*, 3335–3345.
- (50) Qu, L.; Liu, Y.; Baek, J.-B.; Dai, L. *ACS Nano* **2010**, *4*, 1321–1326.

**Supporting Information for “Doping against the native propensity of MoS<sub>2</sub>: degenerate hole doping by cation substitution”**

Joonki Suh,<sup>1</sup> Tae-Eon Park,<sup>2</sup> Der-Yuh Lin,<sup>3</sup> Deyi Fu,<sup>1</sup> Joonsuk Park,<sup>4</sup> Hee Joon Jung,<sup>5</sup> Yabin Chen,<sup>1</sup> Changhyun Ko,<sup>1</sup> Chaun Jang,<sup>2</sup> Yinghui Sun,<sup>6</sup> Robert Sinclair,<sup>4</sup> Joonyeon Chang,<sup>2</sup> Sefaattin Tongay,<sup>1</sup> Junqiao Wu<sup>1,6,\*</sup>

<sup>1</sup> *Department of Materials Science and Engineering, University of California, Berkeley, California 94720, USA*

<sup>2</sup> *Spin Convergence Research Center, Korea Institute of Science and Technology, Seoul 136-791, Korea*

<sup>3</sup> *Department of Electronics Engineering, National Changhua University of Education, Changhua 50007, Taiwan*

<sup>4</sup> *Department of Materials Sciences and Engineering, Stanford University, Stanford, California 94305, USA*

<sup>5</sup> *Energy and Environmental Directorate, Pacific Northwest National Laboratory, Richland, Washington 99352, USA*

<sup>6</sup> *Materials Sciences Division, Lawrence Berkeley National Laboratory, Berkeley, California 94720, USA*

Correspondence and requests for materials should be addressed to J.W. (email: wuj@berkeley.edu).

## Experimental and Analysis Details.

**HRTEM & EFTEM-SI characterization.** After mechanical exfoliation onto a SiO<sub>2</sub>/Si substrate, Nb-doped MoS<sub>2</sub> micro-flakes were transferred to Quantifoil holey carbon-coated Au TEM grids using a polymer-free transfer technique.<sup>1</sup> Cs (spherical aberration)-corrected HRTEM with sub-Å resolution was taken using FEI Titan 80–300 environmental TEM with 80 kV accelerating voltage and a negative spherical aberration coefficient (-20 μm). EFTEM-SI (spectrum image) using JEOL ARM 200cF with GIF Quantum® 965 EELS spectrometer was conducted under these conditions; energy range/slit width/step size: 120–550 eV/10 eV/1 eV and exposure time of a step: 2 sec. Elemental maps of Mo, Nb and S from EFTEM-SI were achieved by energy-filtering at 227 eV (Mo M<sub>4,5</sub>), 378 eV (Nb M<sub>2</sub>), and 165 eV (S L<sub>2,3</sub>), respectively.

**XPS measurements.** XPS was performed on both undoped and Nb-doped MoS<sub>2</sub> utilizing a Mg Kα X-ray source (1253.6 eV) from an anode operated at 300 W and a hemispherical NanoSAM electron energy analyzer in a ultra-high vacuum chamber (base pressure ~ 10<sup>-10</sup> mbar). The samples were directly grounded through metal holders to the system, and the pass energy was kept constant at 10 eV during the scans.

**EXAFS measurements and analysis.** EXAFS measurements at the Nb *K* edge and Mo *K* edge were carried out at the Stanford Synchrotron Radiation Laboratory on beamline 7-3 using a Si (220) monochromator at phi=0°, considering its glitch database in the measured energy range. A Rh-coated Si collimating mirror was used to reject the significant fraction of the higher harmonic signal. Before the measurements, reference Nb and Mo metal foils were also measured for calibration of energy absorption shift. Due to the small amount of Nb dopants, EXAFS data for Nb *K* edge was acquired in a fluorescence geometry using 30-element germanium detector (Canberra). On the contrary, EXAFS of Mo *K* edge was collected in transmission mode where X-ray intensity was measured after passing through the sample using an ionization chamber. Long data collection times (> 8 hrs per measurement) were employed in order to obtain more precise EXAFS signals, and they were averaged in the software package Sixpack after background subtraction. Further data reduction of the EXAFS spectra was processed with Athena, and curve fitting was performed with the Artemis and IFEFFIT software.

**Device fabrication and electrical transport measurements.** All MoS<sub>2</sub> flakes were prepared on 300 nm SiO<sub>2</sub>/Si substrates using mechanical exfoliation. For *p-n* junction devices fabrication, multilayer Nb-doped MoS<sub>2</sub> was directly exfoliated onto a methyl methacrylate (MMA) polymer and transferred to pre-exfoliated undoped MoS<sub>2</sub> sitting on a SiO<sub>2</sub>/Si (*p*<sup>+</sup>) wafer.<sup>2</sup> Standard electron beam lithography was performed twice for patterning the etch mask and the electrodes. XeF<sub>2</sub> etching was used to pattern the Hall-bar configuration, using 4 cycles consisting of 15 sec etch. Ti/Au (5/100 nm) metal contacts were evaporated followed by lift-off. All the electrical transport measurements, excluding the FETs demonstration (Fig. 4a), were performed under vacuum (~ 10<sup>-3</sup> Torr) using a physical property measurement system (PPMS, Quantum Design, Inc.).

The critical hole concentration ( $E_F \sim E_V + 3kT$ ) for degenerate *p*-type MoS<sub>2</sub> is estimated by using a parabolic valence-band model and the corresponding analytical formula,

$$p = 2 \left[ \frac{m_p^* kT}{2\pi\hbar^2} \right]^{3/2} e^{(E_v - E_f)/kT}$$
 . It was found to be approximately  $7 \times 10^{17} \text{ cm}^{-3}$  using a hole effective mass  $m_p^*$  of  $0.68 m_0$ .<sup>3</sup> Therefore, our measured hole density far exceeds this value and justifies our explanation assuming a degenerate doping.

The ideality factor of the p-n junction presented in Fig. 4 is calculated by employing the curve fitting to the Shockley ideal diode equation,  $|I_{ds}| = |I_s| \left( e^{\frac{eV_{ds}}{nk_B T}} - 1 \right)$ . For  $V_g > +40 \text{ V}$  where a significant rectification has been observed, the diode ideality factor ( $n$ ) is found to be  $2 \sim 3$  with  $r^2 > 99\%$ . This presumably implies the existence of charge trap states and disorder either within charge depletion region or at their interfaces.<sup>4</sup>

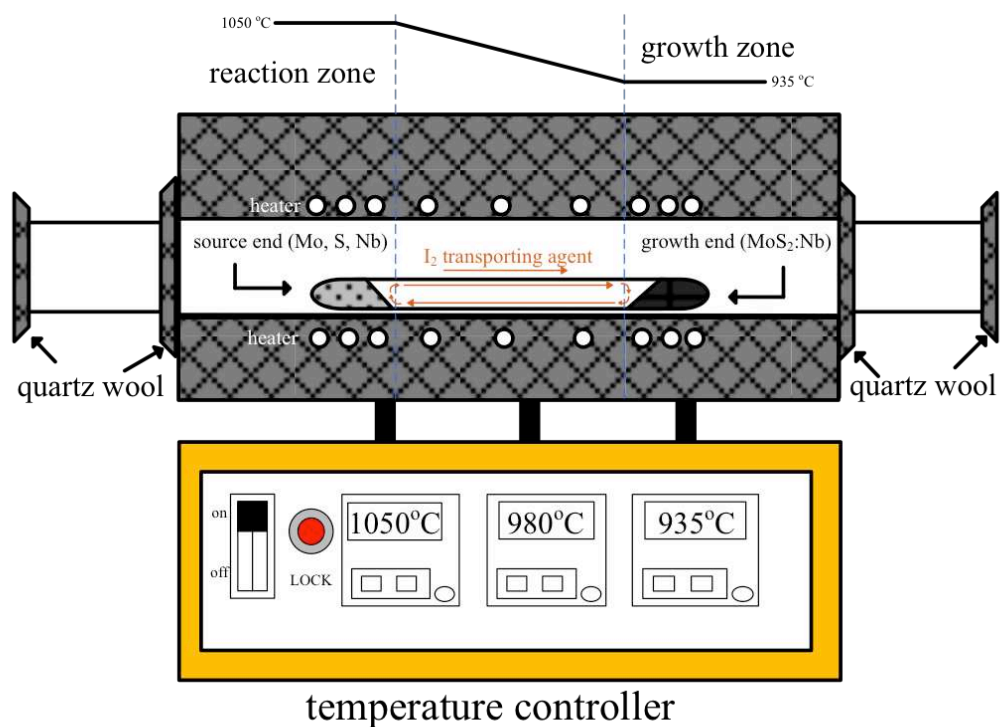


**Figure S1.** Schematics of the three-zone furnace setup used for the Nb-doped MoS<sub>2</sub> crystal growth. Top panel shows the corresponding temperature profile along the horizontal quartz tube during growth process.

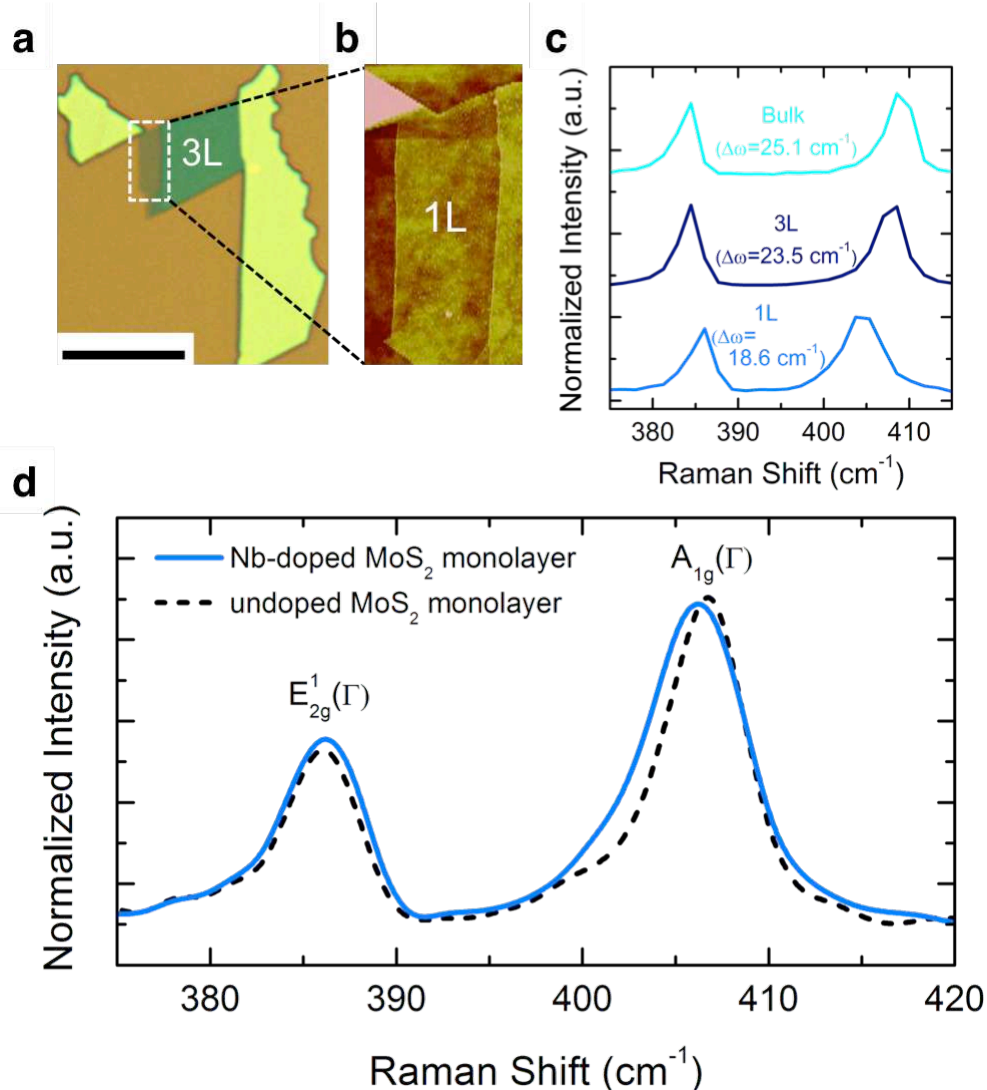


**Figure S2.** (a) Optical image of the as-exfoliated atomic terrace structure consisting of monolayer (1L), trilayer (3L), and bulk MoS<sub>2</sub>:Nb. Scale bar is 10  $\mu\text{m}$ . (b) Zoom-in AFM image of the corresponding monolayer part. (c) Raman spectra, normalized by peak height, of 1L-, 3L-, and bulk MoS<sub>2</sub>:Nb acquired at room temperature. The frequency difference ( $\Delta\omega$ ) between in-plane ( $E_{2g}^1$ ) and out-of-plane ( $A_{1g}$ ) phonon modes at  $\Gamma$  point decreases with the number of layers, and is reduced to  $\sim 18.6 \text{ cm}^{-1}$  in 1L MoS<sub>2</sub>:Nb from the bulk value of  $25.1 \text{ cm}^{-1}$ . (d) Comparison of normalized Raman spectra between Nb-doped and undoped monolayer MoS<sub>2</sub>. We note that the Raman spectral shape slightly changes upon Nb doping (hence greater carrier density); the linewidth of the  $A_{1g}$  mode broadens and slightly softens. In contrast, the  $E_{2g}^1$  mode is insensitive to the Nb doping. This suggests a stronger electron-phonon coupling of the  $A_{1g}$  mode, which is similar to the change in Raman spectrum induced by FET gating.<sup>5</sup> In this regard, Raman spectroscopy can be quite useful for probing the level of doping in 1L-MoS<sub>2</sub> as that is employed in graphene devices.<sup>6,7</sup>

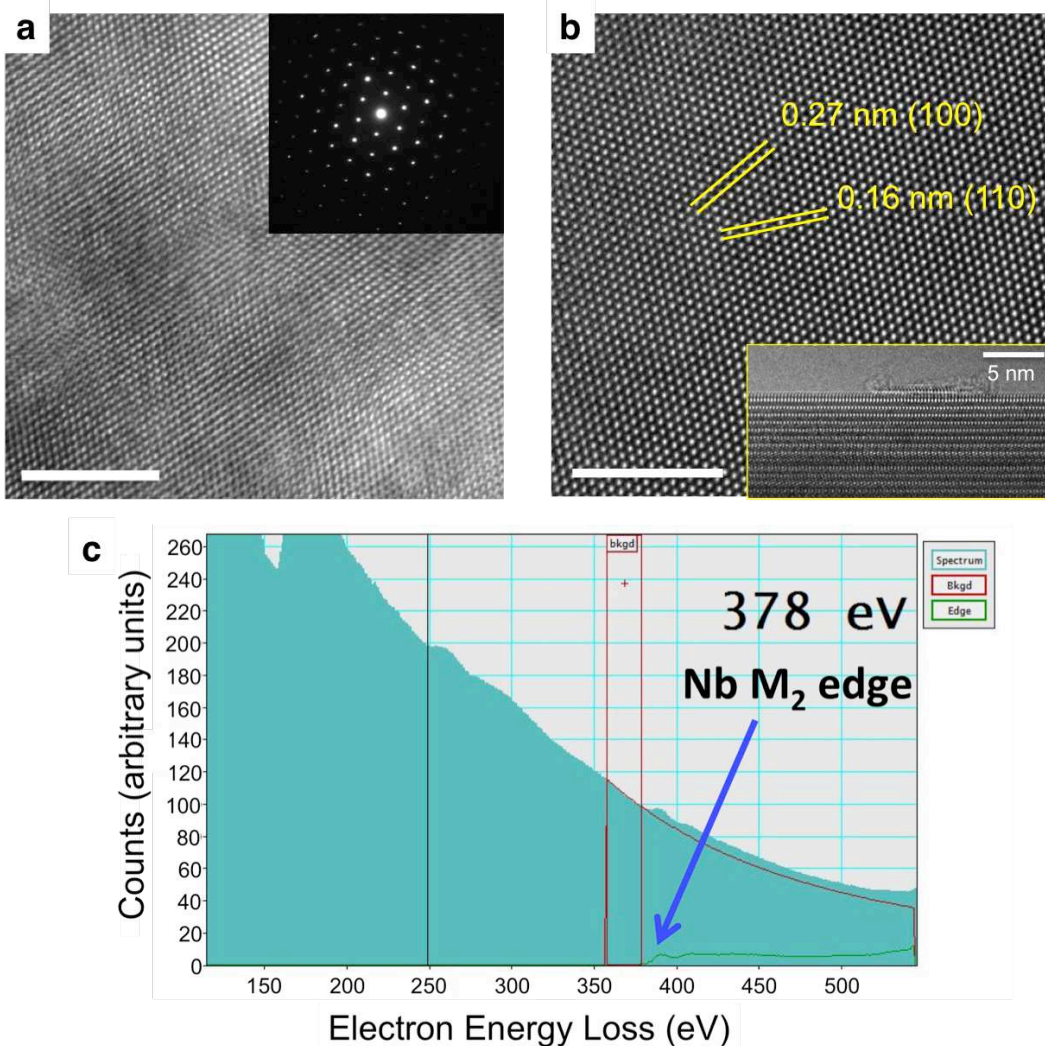


**Figure S3.** (a,b) Additional HRTEM images of a MoS<sub>2</sub>:Nb flake with the selected area electron diffraction pattern acquired and the measured lattice spacing, respectively. Scale bars are 5 nm. Inset in Fig. S3b shows a HRTEM image taken from the MoS<sub>2</sub>:Nb flake with its basal planes oriented in parallel to the electron beam. Estimated inter-plane distance from the image is  $\sim 6.15$  Å, matching well reported value.<sup>8</sup> (c) Extracted electron energy loss spectrum (EELS) from the EFTEM-SI showing the Nb M<sub>2</sub> peak at  $\sim 378$  eV.

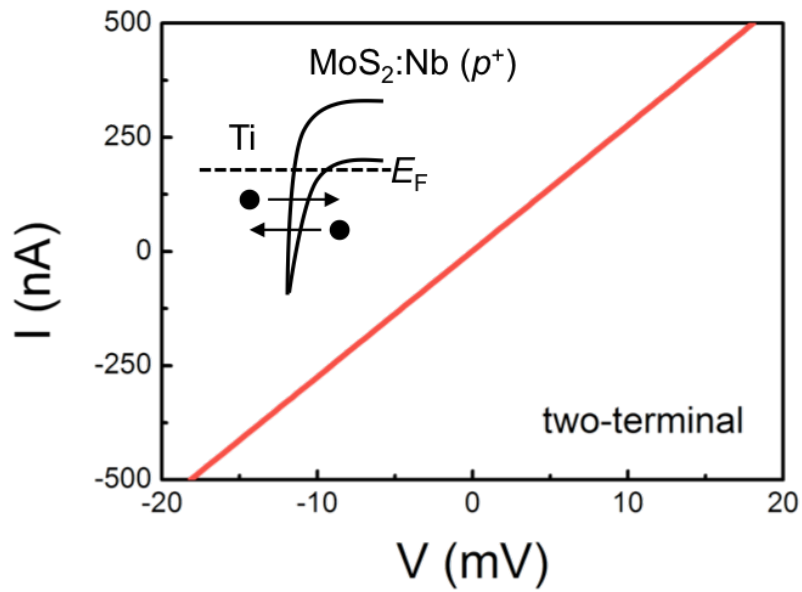


**Figure S4.** Two-terminal  $I$ - $V$  characteristic of the MoS<sub>2</sub>:Nb flake measured at 10 K, showing nature of ohmic contact with Ti. Inset is an expected schematic band diagram across Ti and the degenerate  $p$ -type MoS<sub>2</sub>:Nb, depicting the Schottky barrier overridden by charge tunneling due to the degenerate doping.

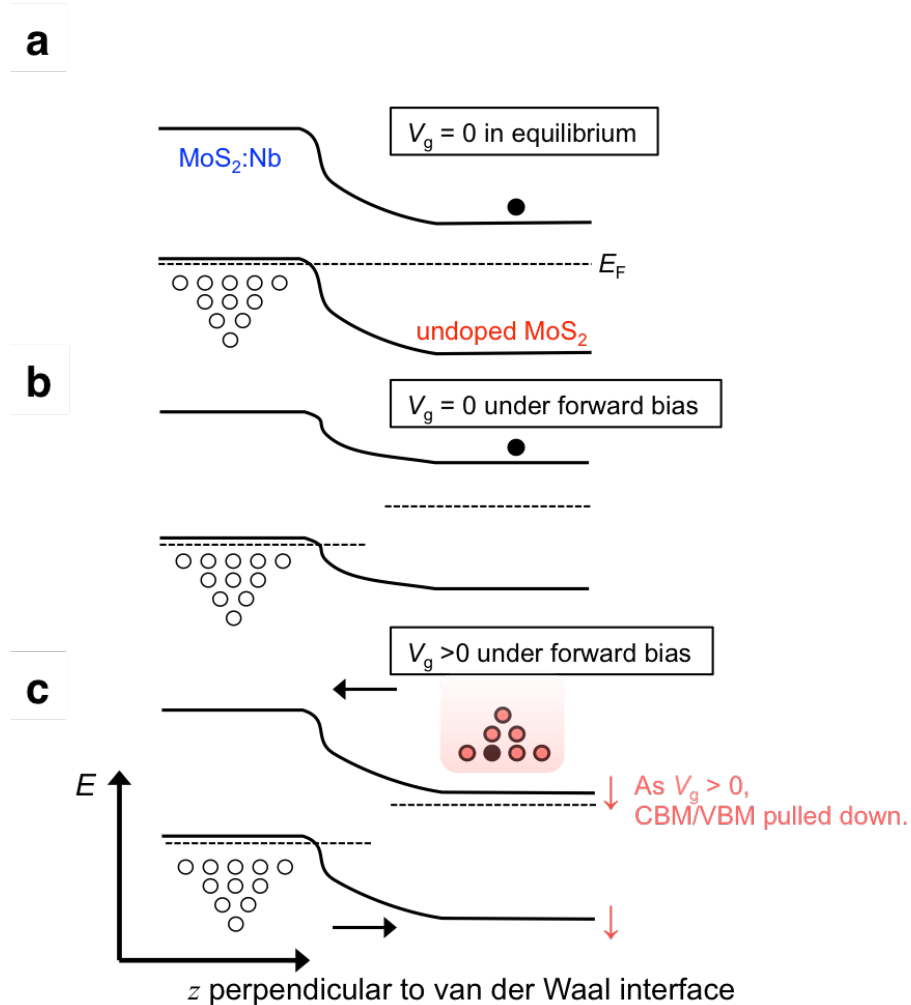


**Figure S5.** Band diagrams across vertical ( $z$ ) MoS<sub>2</sub>  $p$ - $n$  homojunction when no back-gate voltage ( $V_g$ ) is applied in equilibrium state, and under forward bias, respectively (a and b), and a positive  $V_g$  is applied under forward bias (c). Left and right sides correspond to MoS<sub>2</sub>:Nb ( $p$ ) and intrinsic MoS<sub>2</sub> ( $n$ ), respectively. Here, the natural band edge offset between the few-layer ( $\sim 5$  layers) and multilayer ( $\sim 60$  nm) MoS<sub>2</sub> is ignored.<sup>9</sup>

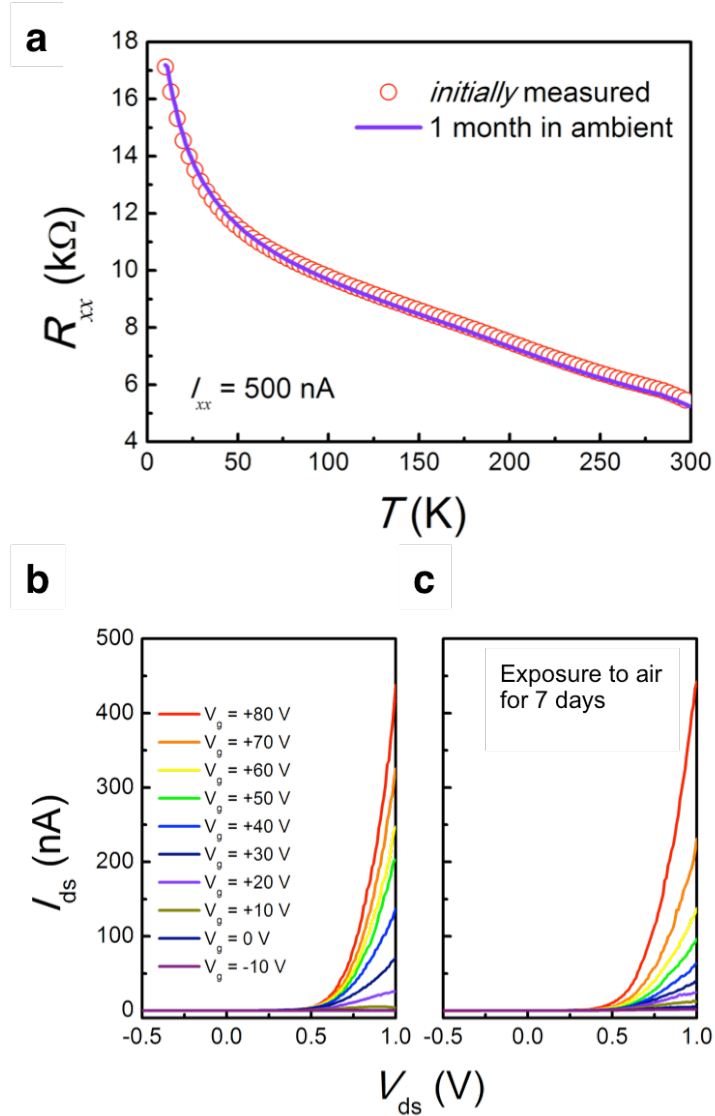


**Figure S6.** (a) Direct evidence of doping stability of a MoS<sub>2</sub>:Nb-based device with comparison of  $R_{xx}$  measured before and after one month in ambient. (b-c) Comparison of  $I$ - $V$  rectification of the MoS<sub>2</sub>:Nb-based diode at various gating voltages before (b) and after (c) 7 days exposure to ambient air.

**Table S1.** EXAFS fitting parameters for Nb-doped MoS<sub>2</sub>.

	1 <sup>st</sup> Peak (Nb–S)			2 <sup>nd</sup> Peak (Nb–Mo/Nb)		
	$N_1$	$r_1$ (Å)	$\sigma_1^2$ (Å <sup>2</sup> )	$N_2$	$r_2$ (Å)	$\sigma_2^2$ (Å <sup>2</sup> )
<b>Nb</b>	6	2.4489	0.00169	6	3.1653	0.00197
	1 <sup>st</sup> Peak (Mo–S)			2 <sup>nd</sup> Peak (Mo–Mo/Nb)		
	$N_1$	$r_1$ (Å)	$\sigma_1^2$ (Å <sup>2</sup> )	$N_2$	$r_2$ (Å)	$\sigma_2^2$ (Å <sup>2</sup> )
<b>Mo</b>	6	2.4042	0.00151	6	3.1394	0.00186

## References

1. Regan, W.; Alem, N.; Alemán, B.; Geng, B.; Girit, Ç.; Maserati, L.; Wang, F.; Crommie, M.; Zettl, A. *Appl. Phys. Lett.* **2010**, *96*, 113102.
2. Ju, L. *et al. Nat. Nanotech.* **2014**, *9*, 348–352.
3. Jin, W. *et al. Phys. Rev. Lett.* **2013**, *111*, 106801.
4. Jariwala, D.; Sangwan, V. K.; Wu, C.-C.; Prabhumirashi, P. L.; Geier, M. L.; Marks, T. J.; Lauhon, L. J.; Hersam, M. C. *Proc. Natl. Acad. Sci. USA* **2013**, *110*, 18076.
5. Chakraborty, B.; Bera, A.; Muthu, D. V. S.; Bhowmick, S.; Waghmare, U. V.; Sood, A. K. *Phys. Rev. B* **2012**, *85*, 161403(R).
6. Pisana, S.; Lazzeri, M.; Casiraghi, C.; Novoselov, K. S.; Geim, A. K.; Ferrari, A. C.; Mauri, F. *Nat. Mater.* **2007**, *6*, 198–201.
7. Das, A. *Nat. Nanotech.* **2008**, *3*, 210–215.
8. Stewart, J. A.; Spearot, D. E. *Modelling Simul. Mater. Sci. Eng.* **2013**, *21*, 045003.
9. Kang, J.; Tongay, S.; Zhou, J.; Li, J.; Wu, J. *Appl. Phys. Lett.* **2013**, *102*, 012111.